Mechanical interaction between additive-manufactured metal lattice structures and bone in compression: implications for stress shielding of orthopaedic implants

Mechanical interaction between additive-manufactured metal lattice structures and bone in compression: implications for stress shielding of orthopaedic implants

Erica Liverani[1], *Giulia Rogati*[2], *Stefania Pagani*[3], *Silvia Brogini*[3,*], *Alessandro Fortunato*[1], *Paolo Caravaggi*[2]

[1] Department of Industrial Engineering, Università di Bologna, Bologna, Italy

[2] IRCCS Istituto Ortopedico Rizzoli, Movement Analysis Laboratory, Bologna, Italy

[3] IRCCS Istituto Ortopedico Rizzoli, Complex Structure of Surgical Sciences and Technologies, Bologna, Italy

∗ Corresponding author:
Silvia Brogini, MSc
IRCCS Istituto Ortopedico Rizzoli
Complex Structure of Surgical Sciences and Technologies
Via Di Barbiano, 1/10
40136 Bologna, Italy
E-mail address: silvia.brogini@ior.it

Abstract

One of the main biomechanical causes for aseptic failure of orthopaedic implants is the stress shielding. This is caused by an uneven load distribution across the bone normally due to a stiff metal prosthesis component, leading to periprosthetic bone resorption and to implant loosening. To reduce the stress shielding and to improve osseointegration, biocompatible porous structures suitable for orthopaedic applications have been developed. Aim of this study was to propose a novel in-vitro model of the mechanical interaction between metal lattice structures and bovine cortical bone in compression. Analysis of the strain distribution between metal structure and bone provides useful information on the potential stress shielding of orthopaedic implants with the same geometry of the porous scaffold. Full density and lattice structures obtained by the repetition of 1.5 mm edge cubic elements via Laser Powder Bed Fusion of CoCrMo powder were characterized for mechanical properties using standard compressive testing. The two porous geometries were characterized by 750 μm and 1000 μm pores resulting in a nominal porosity of 43.5% and 63.2% respectively. Local deformation and strains of metal samples coupled with fresh bovine cortical bone samples were evaluated via Digital Image Correlation analysis up to failure in compression. Visualization and quantification of the local strain gradient across the metal-bone interface was used to assess differences in mechanical behaviour between structures which could be associated to stress-shielding. Overall stiffness and local mechanical properties of lattice and bone were consistent across samples. Full-density metal samples appeared to rigidly transfer the compression force to the bone which was subjected to large deformations (2.2±0.3% at 15kN). Larger porosity lattice was associated to lower stiffness and compressive modulus, and to a smoother load transfer to the bone. While tested on a limited sample size, the proposed in-vitro model appears robust and repeatable to assess the local mechanical interaction of metal samples suitable for orthopaedic applications with the bone tissue. CoCrMo scaffolds made of 1000 μm pores cubic cells may allow for a smoother load transfer to the bone when used as constitutive material of orthopaedic implants.

Keywords

additive manufacturing, lattice structures, stress/strain measurements, stress-shielding, orthopedics, in-vitro model

1. INTRODUCTION

Joint replacement represents the gold-standard surgical treatment to preserve joint motion for post-traumatic or end-stage osteoarthritis. Aging of the population, (Badley and Crotty, 1995) along with the spread of obesity, (Crowson et al., 2013) is associated to the growing prevalence of degenerative osteoarthritis and a significant increase in total hip and knee arthroplasty is expected in the United States in the next twenty years. (Singh et al., 2019) In order to improve patients' quality of life and to decrease the incidence of revision surgeries and implants failure, and thus the economic burden on healthcare systems, clinical research is focusing on innovative designs and materials for endoprostheses. While infections are mostly responsible for early failure of orthopaedic implants, aseptic loosening, instability and osteolysis are those for late failure. (Bozic et al., 2010; Haynes et al., 2016; Le et al., 2014; Sharkey et al., 2013) Stress shielding, or stress protection, is one of the main biomechanical causes of aseptic late failure. This is normally due to the larger stiffness of the implant with respect to that of the adjacent bone, causing periprosthetic bone resorption due to reduced loading at the peri-implant bone. (Huiskes et al., 1992; Nagels et al., 2003; Sumner and Galante, 1992) To reduce the stress shielding and to improve implants' osseointegration, porous and functionally graded structures have been proposed as suitable geometries for orthopaedic implants. (Arabnejad et al., 2017; Chashmi et al., 2020; Hedia et al., 2019; Mahmoud and Elbestawi, 2017) Complex-shape implants can now be obtained via different 3D manufacturing techniques, such as Laser Powder Bed Fusion (LPBF), (Han et al., 2018; Simoneau et al., 2017; Wang et al., 2013; Yan et al., 2015) which allow to print metal lattice structures from 3D CAD models. By modifying the unit cell type, the pores' size and the porosity gradient of the implant-bone lattice interface, the mechanical and functional properties of the orthopaedic implant can be tailored with respect to different anatomical regions and to specific applications (Bandyopadhyay et al., 2010; Van Bael et al., 2012). Cobalt-Chromium-Molybdenum (CoCrMo) and Titanium (Ti6Al4V) alloys are the most widely used materials for endoprostheses and fixation devices (Merola and Affatato, 2019), showing great biocompatibility, positive environment for osteoblast proliferation and suitable mechanical properties to sustain in-vivo physiological loading (Xin et al., 2012; Zhang et al., 2014). While the effect of unit cells geometry and manufacturing parameters on the mechanical behaviour of isolated LPBF-printed CoCrMo (Caravaggi et al., 2019; Hazlehurst et al., 2013, 2014) and Ti6Al4V (Hollander et al., 2006; Zhang et al., 2014) lattice structures was investigated previously, the biomechanical interaction between metal lattice and bone has been seldom investigated, and few robust experimental methodologies reported. Limmahakhun *et al.* have assessed the peri-implant stress shielding in graded cellular CoCrMo scaffolds, using a resin as bone replica and strain gauges to measure local deformations in compression.

(Limmahakhun et al., 2017) In order to overcome the low spatial resolution of strain gauges and the adhesion issues with biological tissues, Digital Image Correlation (DIC) technique has been used for the contactless evaluation of deformations in in-vitro biological models, (Hensley et al., 2017; Palanca et al., 2016; Zhang and Arola, 2004) in particular to assess the mechanical properties of bone specimens. (Acciaioli et al., 2020; Belda et al., 2020; Grassi and Isaksson, 2015; Sztefek et al., 2010; Tayton et al., 2010) Two-dimensional DIC is an optical technique which involves one or more digital cameras for the evaluation of locals displacement and strain of a loaded object by tracking visual differences on the observed surface between the unloaded reference subset and the deformed subset following mechanical loading. (Peters and Ranson, 1982; Sutton et al., 1983) In-silico, finite element modelling (FEM) analysis is an extremely powerful tool to investigate the mechanics of the implant-bone interface, however validation via in-vitro models is always necessary to identify the correct boundary conditions and to provide reference output values for the optimization analysis. A number of in-vitro models have been proposed, but these are often limited in terms of methodology, observed variables and/or in the replica of the real physiological conditions. (Cristofolini and Viceconti, 1999)

The aim of the study is to present a method for the in-vitro evaluation of strain distribution between bovine bone specimens and LPBF-printed porous CoCrMo scaffolds in compression. The CoCrMo lattice structures investigated are characterised by different degrees of porosity via unit cells with hole size in the range of 0.75 - 1 mm, chosen to ensure cell viability, proliferation and colonization (Van Bael et al., 2012). Previous studies on the same structures (Caravaggi et al., 2019; Pagani et al., 2021) confirmed the *in-vitro* biocompatibility and the biological activity of these geometries for orthopaedic applications. A thorough characterization of the lattice structures properties was performed to correlate mechanical behaviour with the manufacturing process. To estimate the mechanical interaction between lattice and bone, which may be correlated to the stress-shielding of implants, an ad-hoc DIC-based setup was designed and implemented across metal samples with different porosities coupled with cortical bone samples.

2. MATERIALS AND METHODS

A procedure for the definition of the geometrical and mechanical properties was established to assess the mechanical interaction between bone and metal samples in compression. Metal and bone samples were individually characterized and, subsequently, the mechanical behaviour of metal-bone sandwiches was evaluated via DIC analysis. Visualization and quantification of the

strain gradient at the metal-bone interface in varying porosity metal lattice and bone samples was used to estimate the effect of lattice porosity on local stress-shielding in compression.

2.1. Samples preparation

2.1.1. CoCrMo lattice structures manufacturing

The lattice samples tested in this study were designed using two types of 1.5 mm edge cubic elements presenting a through hole with diameters of 0.75 mm (S750) and of 1 mm (S1000) respectively (Figure 1a); thus, the nominal structural density (ratio between lattice component and equivalent full density sample) was of 56.5 % and 36.8 %, corresponding to a nominal porosity of 43.5% and 63.2%. For each lattice geometry, three 12 x 12 x 15 mm parallelepipedal samples were produced for the mechanical characterization, and three 9 x 12 x 12 mm samples for the structural tests with the bone samples (Figure 1b).

Lattice samples were fabricated by melting gas-atomized 15-45 μm spherical CoCrMo powder (Carpenter Technology Corporation, Philadelphia, USA; Table 1 for chemical composition) via a LPBF system (SISMA MYSINT100, Vicenza, Italy) equipped with an Yb-Fiber laser (maximum power = 175 W; fixed focused spot diameter = 50 μm). Metal samples were manufactured in a nitrogen-filled chamber with 0.1 % residual oxygen content. MARCAM software (Autofab 2.0) was used to design the lattice samples and to set the laser parameters and the scanning strategy. The scanning strategy was defined as a chessboard where each 0.02 mm thick printing-layer was divided into 3 x 3 mm square blocks. Metal powder was melted in each block in lines spaced by 0.07 mm (meander hatching strategy), and the scanning direction was rotated by 90 deg in adjacent blocks (Figure 1c). Each layer was rotated by 45 deg with respect to the layers above and below. One full density sample with the same dimensions of the lattice was also printed using the same technique.

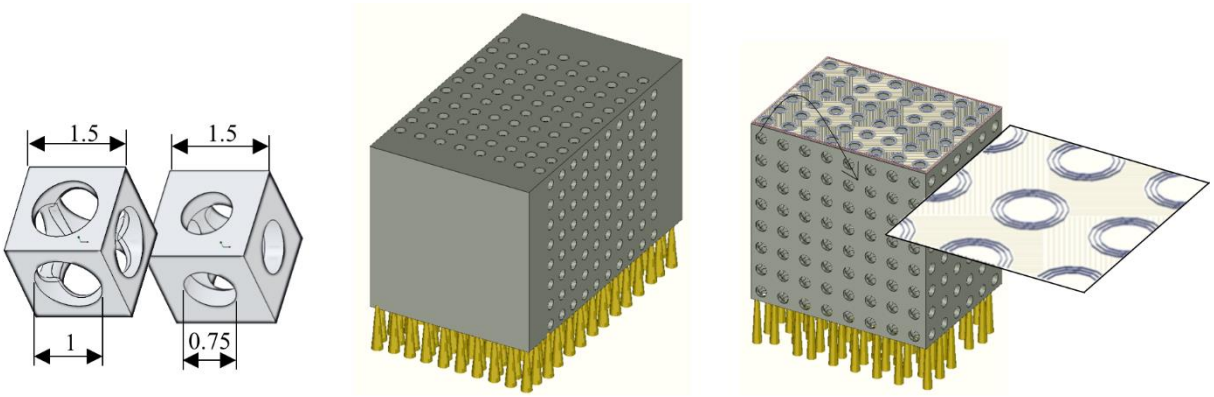

Figure 1: Geometry of CoCr lattice samples. (a) the two cubic units used to create the lattice geometries. (b) S750 sample for mechanical characterization tests and (c) sample for metal-bone sandwiches compression tests. Details of the scanning strategy are shown in (c).

Co	Cr	Mo	Si	Ni	Mn	Fe	C	Ti	W
Balance	27-30	5-7	< 1	0.25-0.50	< 1	< 0.75	< 0.6	< 0.1	< 0.2

Table 1: Chemical composition [wt%] of CoCrMo powder

2.1.2. Bone samples

Fresh bovine bones were obtained from a local butcher. Round samples were extracted from the bone diaphysis using a band-cutting system (EXAKT 310 CP Cutting System, EXAKT Apparatus GmbH, Norderstedt, Germany); these were further reduced with a smaller cutting system (EXAKT 300 CP) for subsequent machining operation. The cutting systems are fitted with water-cooled diamond saw blades allowing precise cuts. The gripping system can oscillate and a feed rate mechanism is present to adjust the cutting speed. 12 x 8 x 11.5 mm cortical bone samples were milled using a 3-axes vertical milling machine (Fidia S.p.A., San Mauro Torinese, Italy), as shown in Figure 2a. Bone samples were stored in a refrigerator at 4 °C in water-soaked tissues to preserve humidity for a maximum of 24 h until compression tests.

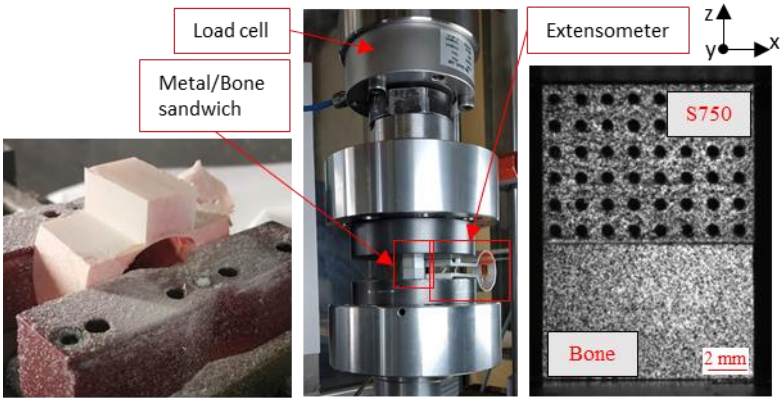

Figure 2: DIC and compression testing setup. (a) Preparation of cortical bone samples via milling. (b) Compression test setup, and (c) random pattern of speckles sprayed on the S750-bone sandwich prepared for DIC analysis.

2.2. Mechanical characterization

2.2.1. Non-destructive tests

Microhardness measurements, microstructural analysis and volume conformity were carried out to assess the main properties of metal samples. Micro-hardness (HV0.5, 15 s dwell time) was measured with a micro-Vickers durometer (HX-1000, Remet) both on the transverse

surface (i.e. the DIC analyzed surface, zx) and on the longitudinal surface (i.e. xy): 15 indentations for each section were carried out using two samples per lattice.

A cross-section parallel to the upper surface of the lattice was obtained for the microstructural characterization. Samples were prepared according to standard practice via mechanical grinding (80–2500 grit papers) and polishing up to 0.6 μm with alumina suspension. Electrochemical etching was performed at 4 V for 20 s, in a solution of hydrochloric acid and ferric chloride dissolved in distilled water (10 mL HCl, 20 g $FeCl_3$, 200 mL H_2O).

Volume conformity was assessed by comparing the real weight of each sample with the nominal weight using the material density. This parameter allows to estimate the average geometrical error due to the manufacturing process. Density was determined following Archimedes' principle, by using an analytical balance to weigh each sample in-air and in-water (precision = ±0.001 g).

2.2.2. Compression tests

Yield Strength (YS) and Ultimate Strength (US) in compression were obtained for isolated metal lattice and cortical bone samples via a uniaxial servo-hydraulic testing machine (Italsigma) fitted with a 100 kN load cell. Bone samples were loaded along the anatomical radial direction, aligned with z axis of the testing machine.

Tests were performed at room temperature with a 0.0005 s^{-1} strain rate. The press control software acquired load data at 10 Hz while the displacement was acquired with an extensometer (Figure 2b).

2.2.3 DIC analysis

DIC analysis was conducted to assess the mechanical interaction between bone and metal samples (full density and lattice), these were coupled in a *sandwich* configuration and tested (Figure 2c) in compression using DIC. A random pattern of speckles was artificially created by spraying the lateral surface of the samples with black paint on a white background (Figure 2c). A custom LabVIEW program was used to store camera frames (6.4 MPx Basler acA3088-57μm) which were recorded at constant steps of 1 ± 0.5 kN. GOM Correlate (version 2.0.1, Braunschweig, Germany) was used to elaborate the images in order to measure local displacements and local strain of each pixel identified in a user-defined area, which was the same for each frame. The following parameters were extracted: the overall stiffness of the sandwich structure (k_{TOT}), the stiffness of each lattice layer - i.e. unit cells at the same z-level - (k_L), an indirect calculation of the stiffness of single units (k_U) and a map of local strains

concentration. k_{TOT} is the mean across all $k_{TOT,i}$, where the latter is the ratio between the load at the i^{th} frame and the corresponding total displacement; k_U is the mean across all $k_{U,i-m}$, where the latter is the ratio between the load at the i^{th} frame and every m^{th} layer displacement. In case of full density metal and bone samples, the volume was virtually divided into 1.5 mm side cubes to allow comparison of k_U with that of porous samples.

3. RESULTS

3.1 Non-destructive characterization of lattice

Microhardness measurements are reported in Figure 3, and were compared with minimum (Tonelli et al., 2020) and maximum (Qian et al., 2015) values reported in literature.

The average microhardness was in the range 410-490 HV0.5. The distance y from the building platform did not seem to affect microhardness. Similarly, transverse and longitudinal cross sections did not show significant differences in hardness in both full density and lattice samples, despite the intrinsic anisotropy of LPBF-built components.

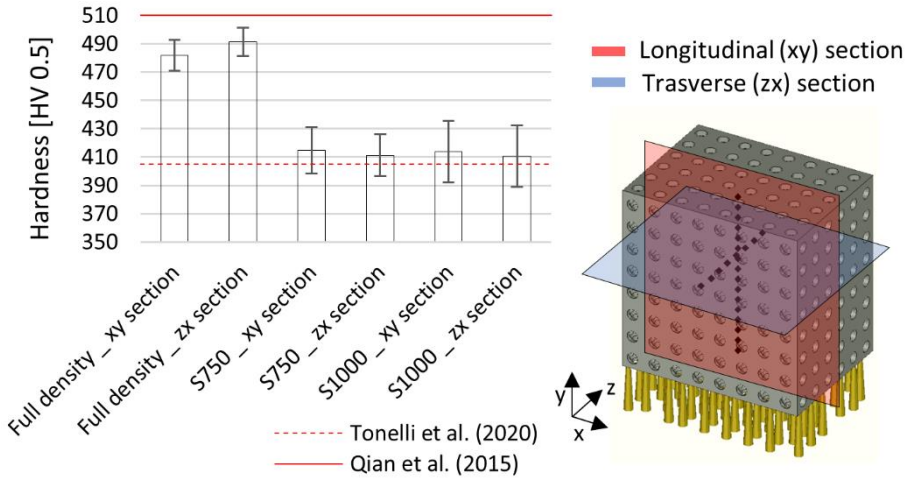

Figure 3: Hardness measurements. HV0.5 Hardness measurement on transverse and longitudinal section of full density and lattice samples.

Electrochemical etching of polished cross-sections and following observation under polarized light microscopy revealed a texture showing preferential solidification and columnar grain growth in the building direction (Figure 4 a, c, d).

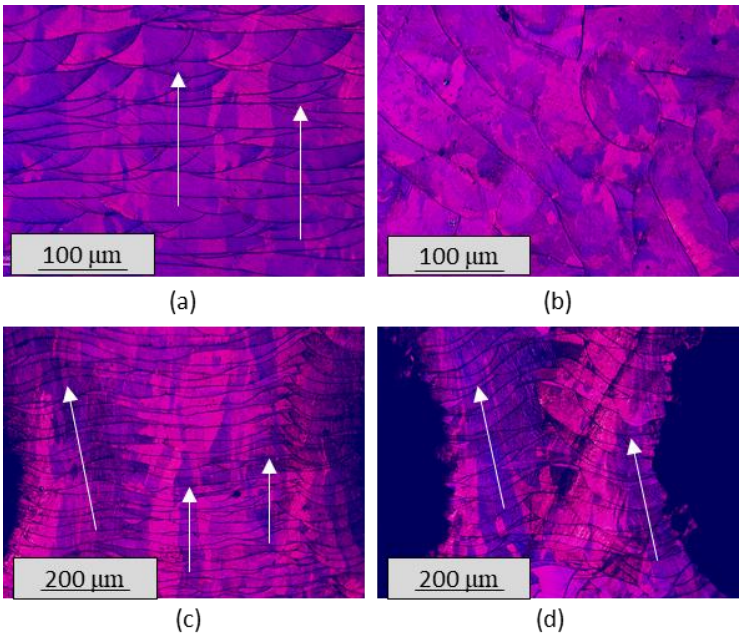

Figure 4: Polarized light micrographs of metal samples. Micrographs under polarized light of the full-density metal sample along the building (a) and transverse (b) directions, and of S750 (c) and S1000 (d) lattice structures along the building direction.

The full density sample, conversely, presented significantly higher hardness by 75 HV0.5 than the lattices.

A small difference in density was observed in the LPBF samples (8.26 g*cm^{-3}) with respect to the nominal density of CoCrMo produced by conventional investment casting (8.30 g*cm^{-3}, ASTM F75-12; UNS R30075), which may indicate the presence of internal defects and/or pores. Defects analysis was beyond this work, and the real density was used to estimate the difference in volume between nominal and real components. The mean volumetric error was 3.8 % for the S750 lattice and 4.2 % for the S1000.

3.2 Compression tests and DIC analysis

The compressive stress-engineering strains of isolated S750, S1000 lattice and cortical bone samples are presented in Figure 5a. The plot displays the stress-strain behaviour of lattices until failure of the first layer, and until sudden failure of any part of the bone samples. Stress is reported as equivalent-stress, the ratio between the applied load and the maximum surface of 144 mm^2 (12 x 12 mm). Figure 5b shows the DIC-estimated local strain map (ε_z, along the loading direction) at 15.3 kN in the lattice and bone samples highlighting the different deformation values reached by the two materials. The cortical bone reached a local peak deformation of 8%, S1000 of 2.5% and S750 of about 0.8%. The global strain, corresponding to a stress of 105-123 MPa, were of 1.8%, 1.45% and 0.45%, respectively for bone, S1000 and

S750 (Figure 5a). These values were approximately 22%, 56% and 56% of the maximum local strain.

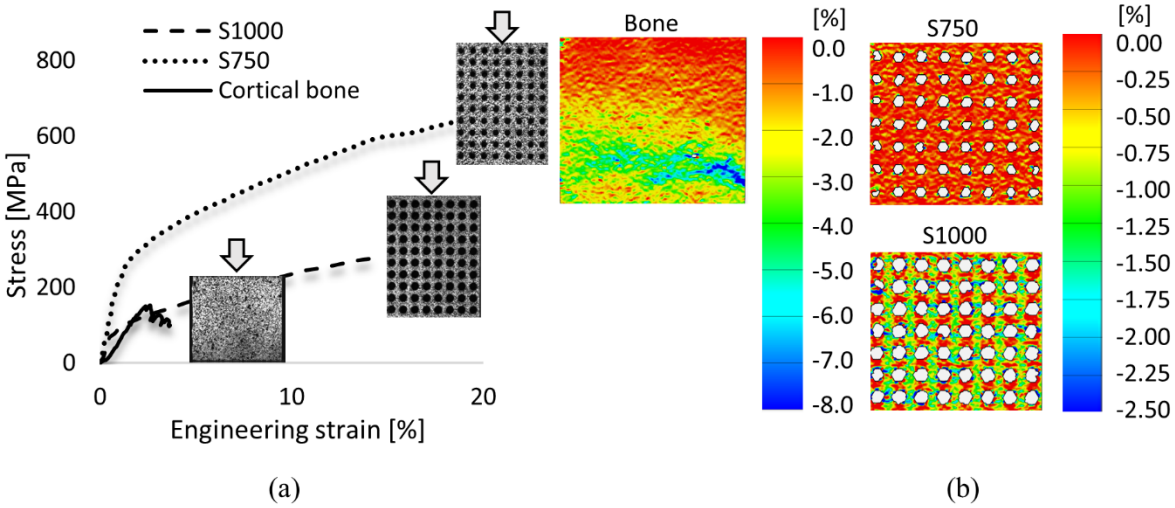

Figure 5: Strain of bone and metal samples in compression. (a) Compressive stress-engineering strain curve of cortical bone and of the two lattice geometries, and (b) DIC-based local strain analysis of one exemplary sample for bone and metal lattices at 15.3 kN.

Young's Modulus, YS and US in compression (or Compressive Proof Strength) of lattice samples (ISO 13314 - 2016) are reported in Table 2. Reference mechanical properties for full-density CoCrMo samples (mean values and standard deviations) in compression were reported previously (Liverani et al., 2016) and can be summarized as follows: Young's Modulus of 193 (16.7) GPa, YS of 742 (21.5) MPa and US of 882 (67.6) MPa.

	Young's Modulus [GPa]	Mean (Std)	YS [MPa]	Mean (Std)	US [MPa]	Mean (Std)
S750_1	22.8	23.2 (1.3)	225	246.7 (20.2)	658	653.3 (3.5)
S750_2	22.1		265		654	
S750_3	24.6		250		651	
S1000_1	14.7	13.6 (4.0)	90	88.3 (7.6)	291	289.3 (9.6)
S1000_2	9.1		95		279	
S1000_3	16.9		80		298	
Bone_1	8.7		122		123	
Bone_2	8.1		145		152	

Table 2: Mean mechanical properties (standard deviations) in compression of metal lattice and cortical bone samples.

Figure 6 is displaying an exemplary output from the compression test of one sandwich structure analysed by DIC. The displacement map shows full density CoCrMo sample coupled with the

bone subjected to 10 kN compressive load and observed in the zx surface. Similar maps of both lattices and bone samples were obtained at each load step; the displacement in the mid zx section was used as reference for stiffness estimation (Figure 6a,b). As predictable, the full density metal sample presented a much lower displacement (0.006 mm) with respect to the cortical bone (0.104 mm) at 10 kN (Figure 6a,b).

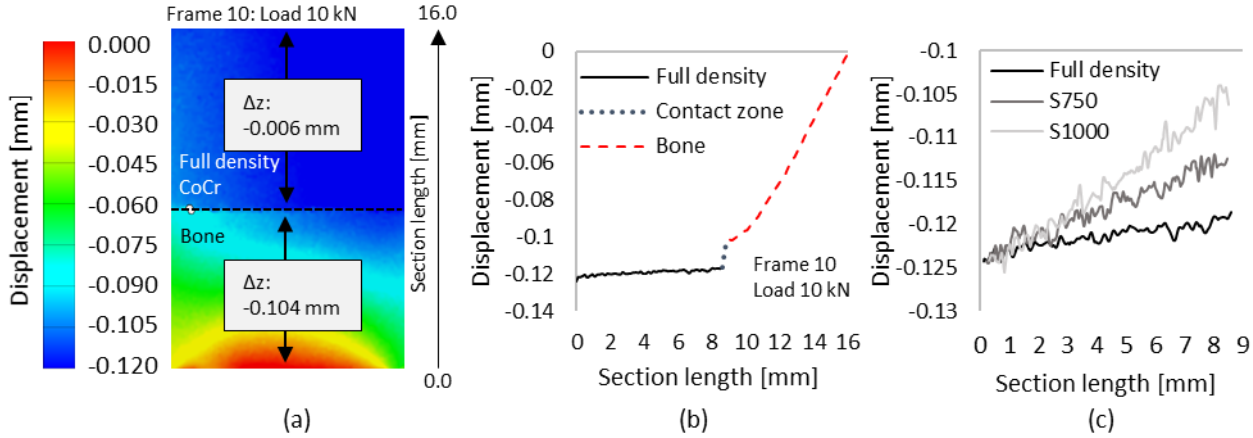

Figure 6: Displacement of compressed metal-bone sandwiches. (a) Color map of local displacement and (b) displacement along the mid zx section of a full-density metal-bone sandwich. (c) Displacement of all metal samples coupled with bone at the same load.

Figure 6c shows the comparison between full density and lattice samples displacements at 10 kN: the displacement of metal samples progressively increases from the full density sample (0.006 mm) to the two porous scaffold structures S750 (0.012 mm) and S1000 (0.018 mm). The displacement of the single parts was associated to the strain behaviour of the metal-bone sandwich. Figure 7 compares the maximum deformation recorded in all sandwiches at 14-15 kN. In the full density metal-bone and in the S750-bone sandwiches, the deformation occurs mainly in the bone, with an average 2.2±0.3% deformation recorded (2.05% in the specific bone sample shows in Figure 7); corresponding engineering strain of 0.04% and 0.15% were observed in the metal samples. Conversely, in the S1000-bone sandwich, the lattice structure presented a mean deformation of 0.91% in the same loading conditions.

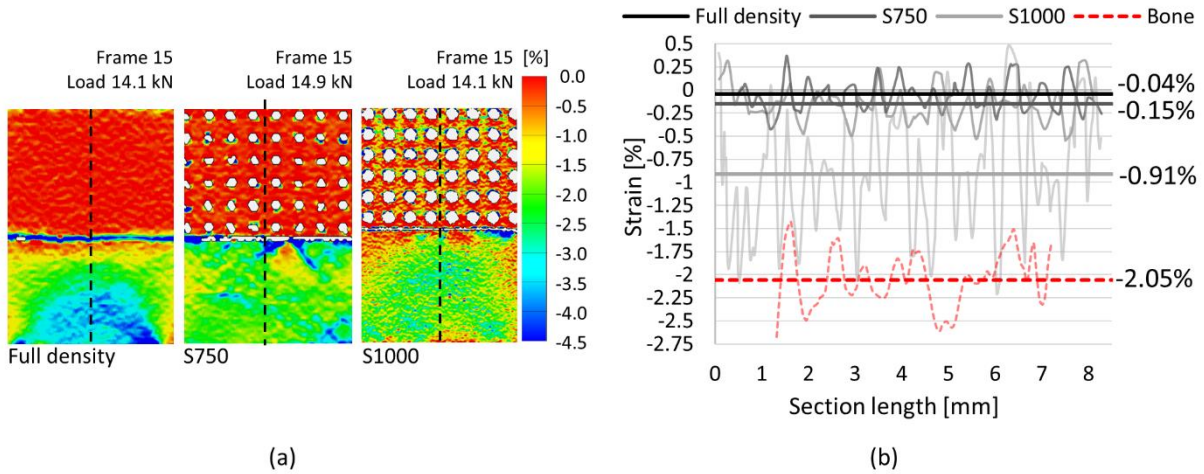

Figure 7: DIC-based strain map in the three metal-bone sandwiches. (a) Color map of local strain in CoCrMo-bone sandwiches at 14-15 kN compressive load, and (b) strains observed along the mid-section - dashed line in (a) - of metal and bone samples. Mean strains across the sandwich section are shown as straight lines.

The displacement of each layer was measured at all applied loads (up to YS). Once k_L has been measured for each lattice layer, k_U can be calculated using the parallel and series springs theory. Table 3 is reporting mean stiffness values across all bone and metal samples.

Sample	CoCrMo k_{TOT} (Std) [kN/mm]	CoCrMo k_L (Std) [kN/mm]	CoCrMo k_U [kN/mm]	Bone k_{TOT} (Std.) [kN/mm]	Bone k_U (Std) [kN/mm]
Full density-bone	1492	7908	124	109 (17.2)	9.9 (1.9)
S750-Bone	1020 (132.2)	5605 (265.6)	88		
S1000-Bone	926 (25.9)	3387(61.2)	53		

Table 3: Total stiffness, single layer stiffness and single unit stiffness of metal and bone samples.

4. DISCUSSION

Orthopaedic implants, such as prosthesis components or fixation plates, are used to replace disrupted joints and to reduce and stabilize bone fractures. Analysis of the mechanical interaction between these metal devices, which are mostly made in biocompatible metal alloys,

and human bone, requires complex in-silico and in-vitro models. One of the main reasons for the aseptic loosening failure of endoprostheses is the stress-shielding, which is due to differences in stiffness between implant and adjacent bone causing regions of stress concentration and of stress relief leading to bone resorption. (Wolff, 1893) While in-silico models and FEM analyses are extremely valuable and flexible tools to estimate stress and strain distribution at the implant-bone interface, these require in-vitro experimental data to establish the mechanical properties and for optimization of the boundary conditions. Complex-shape 3D-printed metal porous structures are increasingly showing potential applications in orthopaedics, but their mechanical interaction with biological tissue is difficult to predict. Analysis of the stress shielding is most commonly performed on full implants either via in-silico (Alkhatib et al., 2019; Oshkour et al., 2013) or in-vitro models (Arabnejad et al., 2017; Cristofolini and Viceconti, 1999) subjected to complex loading conditions, thus the outcome is sensitive to several parameters and may be affected by large errors (Cristofolini and Viceconti, 1999). Therefore, in order to improve the control of the loading conditions at the local level, this study aimed at proposing a simple in-vitro model of the mechanical interaction between small geometrical units of an orthopaedic implant and of bovine cortical bone in just one loading direction. This model has allowed to get a better insight into the local strain distribution at the implant-bone interface in compression, thus helped to disclose novel information on the main parameters characterizing the stress-shielding phenomenon.

In terms of material properties, YS and Young modulus of the cortical bone samples estimated here are consistent with what reported in the literature for bovine bone tissue. (Nobakhti et al., 2017) Properties of lattice were consistent across samples and, as predictable, larger porosity was associated to lower stiffness and lower compressive modulus. In fact, the proposed methodology allowed to estimate the stiffness of single unit cells comprising the lattice, which could be compared to that of the bone with the same dimensions. This information may help establishing the correct dimensions, and thus the overall mechanical behaviour, of lattice structures for an optimized implant-to-bone strain distribution. Type and size of unit cells, and the number of layers comprising the scaffold, significantly affect the total stiffness of the lattice which can therefore be optimally designed for the required application. DIC analysis of the sandwiches in compression has allowed to quantify and to visually appreciate the stiffness gradient at the metal-bone interface. The full-density metal sample paired with cortical bone appeared to rigidly transfer the compression force to the bone, which is subjected to large deformation along the force direction (Figures 6 and 7). Significantly lower deformations were observed in the bone when coupled with the S1000 lattice. This showed much larger average

strains across the layers (about 1%) with respect to the full density and the S750 in similar loading conditions (Figure 7b). The unit stiffness ratio between bone and metal samples increases by an order of magnitude decreasing the structures density, with a difference in the range 8-18.7% between full density and S1000. From a stress-shielding standpoint, the S1000 lattice would therefore appear to be a more suitable constitutive material for the implant-bone interface allowing a smoother load transfer to the adjacent bone. When implemented in an orthopaedic implant, this smooth load transfer should reduce regions of high and low stress concentrations which may lead to bone resorption (Wolff, 1893) and consequently to implant loosening. The benefit of using a porous structure at the implant-bone interface is double-fold: it would also improve osseointegration allowing vascularized bone tissue to grow within the implant pores thus providing stronger secondary stabilization.

The mechanical properties of lattice samples were strongly associated to the manufacturing process and the building direction of the components was shown to affect the isotropic behavior. Small but significant differences in US and compressive modulus were observed with respect to same-geometry scaffolds (S750) tested previously, (Pagani et al., 2021) built along a direction orthogonal to that used in the present study. Optical images clearly show the typical microstructure pattern of LPBF components with columnar grains oriented along the building direction, while only globular grains are visible on the orthogonal surface. Microhardness does not appear to be affected by the distance from the platform or it may be difficult to reveal due to the relatively low height of the present samples. The full density sample however presented a hardness 75 HV0.5 larger than that of the lattices. This may be due to differences in conduction affecting the cooling rate and thus the superficial mechanical properties. As highlighted in detail in a previous study by the same authors, (Caravaggi et al., 2019) the LPBF process results in some geometric variations with respect to the nominal 3D lattice shapes. In this study, a low difference (+ 3-4%) was observed with respect to the nominal mean volume of lattice structures.

The outcome of this study should be interpreted with respect to some limitations. DIC analysis was conducted on a limited number of bone and metal samples. While the estimated local and global mechanical properties of single and sandwich structures were consistent, a larger sample size would be required to confirm these data. The bovine bone tissue used here is considered a good biological replicate of the human cortical bone, (Morgan et al., 2018) however the latter has a larger elastic modulus (around 18 GPa). Therefore, the measured difference in stiffness between porous samples and bone observed here could be slightly lower in case of human tissue, which may result in better strain distribution and lower stress shielding. Porous Ti6Al4V

structures can also be used and tested in the future to reduce the stress shielding. However, its lower elastic modulus (110 GPa) and compressive strength make the full-density material – and therefore its porous lattices - not fully suitable for orthopaedic implants such as hip, knee and ankle endoprostheses which must sustain up to body weights (around 7 KN) in dynamic activities. Finally, the proposed model has been assessed in compression only and the interaction between lattice and bone has been evaluated with ideal full contact surfaces. Future endeavours should therefore focus on replicating the physiological multi-planar loading conditions of orthopaedic implants; these may be applied to human bone specimens and assessed via DIC 3D to extend the deformation analysis to the whole 3D sandwich structure.

5. CONCLUSIONS

The present study is reporting a simple DIC-based model for the quantitative evaluation of the strain distribution at the implant-bone interface of orthopaedic implants. The methodology has proved repeatable but requires further validation on a larger sample size. According to the present outcome, CoCrMo scaffolds made of 1000 μm pores cubic cells may allow for a smoother load transfer to the bone when used as constitutive material of orthopaedic implants, which could result in lower stress-shielding with respect to a full-density metal implant.

AUTHOR CONTRIBUTION

E. Liverani: Methodology, Investigation, Writing – Original Draft; G. Rogati: Methodology, Data Curation, Writing – Original Draft; S. Pagani: Methodology, Writing – Review & editing; S. Brogini: Resources, Writing – Review & editing; A. Fortunato: Resources, Supervision; P. Caravaggi: Conceptualization, Methodology, Writing – Review & editing. All authors read and approved the submitted manuscript version.

ACKNOWLEDGMENT

The authors are grateful to Rizzoli Orthopaedic Institute (funds 5 × 1000, year 2017; Cod. 730171).

REFERENCES

Acciaioli, A., Falco, L., Baleani, M., 2020. Measurement of apparent mechanical properties of trabecular bone tissue: Accuracy and limitation of digital image correlation technique. J.

Mech. Behav. Biomed. Mater. 103, 103542. https://doi.org/10.1016/j.jmbbm.2019.103542

Alkhatib, S.E., Tarlochan, F., Mehboob, H., Singh, R., Kadirgama, K., Harun, W.S.B.W., 2019. Finite element study of functionally graded porous femoral stems incorporating body-centered cubic structure. Artif. Organs 43, E152–E164. https://doi.org/10.1111/aor.13444

Arabnejad, S., Johnston, B., Tanzer, M., Pasini, D., 2017. Fully porous 3D printed titanium femoral stem to reduce stress-shielding following total hip arthroplasty. J. Orthop. Res. 35, 1774–1783. https://doi.org/10.1002/jor.23445

Badley, E.M., Crotty, M., 1995. An international comparison of the estimated effect of the aging of the population on the major cause of disablement, musculoskeletal disorders. J. Rheumatol. 22, 1934–1940.

Bandyopadhyay, A., Espana, F., Balla, V.K., Bose, S., Ohgami, Y., Davies, N.M., 2010. Influence of porosity on mechanical properties and in vivo response of Ti6Al4V implants. Acta Biomater. 6, 1640–1648.

Belda, R., Palomar, M., Peris-Serra, J.L., Vercher-Martínez, A., Giner, E., 2020. Compression failure characterization of cancellous bone combining experimental testing, digital image correlation and finite element modeling. Int. J. Mech. Sci. 165, 105213. https://doi.org/10.1016/j.ijmecsci.2019.105213

Bozic, K.J., Kurtz, S.M., Lau, E., Ong, K., Chiu, V., Vail, T.P., Rubash, H.E., Berry, D.J., 2010. The epidemiology of revision total knee arthroplasty in the United States. Clin. Orthop. Relat. Res. 468, 45–51.

Caravaggi, P., Liverani, E., Leardini, A., Fortunato, A., Belvedere, C., Baruffaldi, F., Fini, M., Parrilli, A., Mattioli-Belmonte, M., Tomesani, L., Pagani, S., 2019. CoCr porous scaffolds manufactured via selective laser melting in orthopedics: Topographical, mechanical, and biological characterization. J. Biomed. Mater. Res. - Part B Appl.

Biomater. 107, 2343–2353. https://doi.org/10.1002/jbm.b.34328

Chashmi, M.J., Fathi, A., Shirzad, M., Jafari-Talookolaei, R.A., Bodaghi, M., Rabiee, S.M., 2020. Design and analysis of porous functionally graded femoral prostheses with improved stress shielding. Designs 4, 1–15. https://doi.org/10.3390/designs4020012

Cristofolini, L., Viceconti, M., 1999. In vitro stress shielding measurements can be affected by large errors. J. Arthroplasty 14, 215–219. https://doi.org/10.1016/S0883-5403(99)90129-8

Crowson, C.S., Matteson, E.L., Davis, J.M., Gabriel, S.E., 2013. Contribution of obesity to the rise in incidence of rheumatoid arthritis. Arthritis Care Res. 65, 71–77. https://doi.org/10.1002/acr.21660

Grassi, L., Isaksson, H., 2015. Extracting accurate strain measurements in bone mechanics: A critical review of current methods. J. Mech. Behav. Biomed. Mater. 50, 43–54. https://doi.org/10.1016/j.jmbbm.2015.06.006

Han, C., Li, Y., Wang, Q., Wen, S., Wei, Q., Yan, C., Hao, L., Liu, J., Shi, Y., 2018. Continuous functionally graded porous titanium scaffolds manufactured by selective laser melting for bone implants. J. Mech. Behav. Biomed. Mater. 80, 119–127. https://doi.org/10.1016/j.jmbbm.2018.01.013

Haynes, J.A., Stambough, J.B., Sassoon, A.A., Johnson, S.R., Clohisy, J.C., Nunley, R.M., 2016. Contemporary Surgical Indications and Referral Trends in Revision Total Hip Arthroplasty: A 10-Year Review. J. Arthroplasty 31, 622–625. https://doi.org/10.1016/j.arth.2015.09.026

Hazlehurst, K., Wang, C.J., Stanford, M., 2013. Evaluation of the stiffness characteristics of square pore CoCrMo cellular structures manufactured using laser melting technology for potential orthopaedic applications. Mater. Des. 51, 949–955. https://doi.org/10.1016/j.matdes.2013.05.009

Hazlehurst, K.B., Wang, C.J., Stanford, M., 2014. An investigation into the flexural

characteristics of functionally graded cobalt chrome femoral stems manufactured using selective laser melting. Mater. Des. 60, 177–183. https://doi.org/10.1016/j.matdes.2014.03.068

Hedia, H.S., Aldousari, S.M., Timraz, H.A., Fouda, N., 2019. Stress shielding reduction via graded porosity of a femoral stem implant. Mater. Test. 61, 695–704. https://doi.org/10.3139/120.111374

Hensley, S., Christensen, M., Small, S., Archer, D., Lakes, E., Rogge, R., 2017. Digital image correlation techniques for strain measurement in a variety of biomechanical test models. Acta Bioeng. Biomech. 19, 187–195. https://doi.org/10.5277/ABB-00785-2016-04

Hollander, D.A., Von Walter, M., Wirtz, T., Sellei, R., Schmidt-Rohlfing, B., Paar, O., Erli, H.-J., 2006. Structural, mechanical and in vitro characterization of individually structured Ti–6Al–4V produced by direct laser forming. Biomaterials 27, 955–963.

Huiskes, R., Weinans, H., Van Rietbergen, B., 1992. The relationship between stress shielding and bone resorption around total hip stems and the effects of flexible materials. Clin. Orthop. Relat. Res. 124–134. https://doi.org/10.1097/00003086-199201000-00014

Le, D.H., Goodman, S.B., Maloney, W.J., Huddleston, J.I., 2014. Current modes of failure in TKA: Infection, instability, and stiffness predominate. Clin. Orthop. Relat. Res. 472, 2197–2200. https://doi.org/10.1007/s11999-014-3540-y

Limmahakhun, S., Oloyede, A., Sitthiseripratip, K., Xiao, Y., Yan, C., 2017. Stiffness and strength tailoring of cobalt chromium graded cellular structures for stress-shielding reduction. Mater. Des. 114, 633–641. https://doi.org/10.1016/j.matdes.2016.11.090

Liverani, E., Fortunato, A., Leardini, A., Belvedere, C., Siegler, S., Ceschini, L., Ascari, A., 2016. Fabrication of Co-Cr-Mo endoprosthetic ankle devices by means of Selective Laser Melting (SLM). Mater. Des. 106, 60–68. https://doi.org/10.1016/j.matdes.2016.05.083

Mahmoud, D., Elbestawi, M., 2017. Lattice Structures and Functionally Graded Materials

Applications in Additive Manufacturing of Orthopedic Implants: A Review. J. Manuf. Mater. Process. 1, 13. https://doi.org/10.3390/jmmp1020013

Merola, M., Affatato, S., 2019. Materials for hip prostheses: A review of wear and loading considerations. Materials (Basel). 12, 495.

Morgan, E.F., Unnikrisnan, G.U., Hussein, A.I., 2018. Bone Mechanical Properties in Healthy and Diseased States. Annu. Rev. Biomed. Eng. 20, 119–143. https://doi.org/10.1146/annurev-bioeng-062117-121139

Nagels, J., Stokdijk, M., Rozing, P.M., 2003. Stress shielding and bone resorption in shoulder arthroplasty. J. Shoulder Elb. Surg. 12, 35–39. https://doi.org/10.1067/mse.2003.22

Nobakhti, S., Katsamenis, O.L., Zaarour, N., Limbert, G., Thurner, P.J., 2017. Elastic modulus varies along the bovine femur. J. Mech. Behav. Biomed. Mater. 71, 279–285. https://doi.org/10.1016/j.jmbbm.2017.03.021

Oshkour, A.A., Osman, N.A.A., Yau, Y.H., Tarlochan, F., Abas, W.A.B.W., 2013. Design of new generation femoral prostheses using functionally graded materials: A finite element analysis. Proc. Inst. Mech. Eng. Part H J. Eng. Med. 227, 3–17. https://doi.org/10.1177/0954411912459421

Pagani, S., Liverani, E., Giavaresi, G., De Luca, A., Belvedere, C., Fortunato, A., Leardini, A., Fini, M., Tomesani, L., Caravaggi, P., 2021. Mechanical and in vitro biological properties of uniform and graded cobalt-chrome lattice structures in orthopedic implants. J. Biomed. Mater. Res. part B - Appl. Biomater.

Palanca, M., Tozzi, G., Cristofolini, L., 2016. The use of digital image correlation in the biomechanical area: A review. Int. Biomech. 3, 1–21. https://doi.org/10.1080/23335432.2015.1117395

Peters, W.H., Ranson, W.F., 1982. Digital Imaging Techniques In Experimental Stress Analysis. Opt. Eng. 21, 213427. https://doi.org/10.1117/12.7972925

Qian, B., Saeidi, K., Kvetková, L., Lofaj, F., Xiao, C., Shen, Z., 2015. Defects-tolerant Co-Cr-

Mo dental alloys prepared by selective laser melting. Dent. Mater. 31, 1435–1444. https://doi.org/10.1016/j.dental.2015.09.003

Sharkey, P.F., Lichstein, P.M., Shen, C., Tokarski, A.T., Parvizi, J., 2013. Why are total knee arthroplasties failing today-has anything changed after 10 years? J. Arthroplasty 29, 1774–1778. https://doi.org/10.1016/j.arth.2013.07.024

Simoneau, C., Terriault, P., Jetté, B., Dumas, M., Brailovski, V., 2017. Development of a porous metallic femoral stem: Design, manufacturing, simulation and mechanical testing. Mater. Des. 114, 546–556. https://doi.org/10.1016/j.matdes.2016.10.064

Singh, J.A., Yu, S., Chen, L., Cleveland, J.D., 2019. Rates of total joint replacement in the United States: Future projections to 2020-2040 using the national inpatient sample. J. Rheumatol. 46, 1134–1140. https://doi.org/10.3899/jrheum.170990

Sumner, D.R., Galante, J.O., 1992. Determinants of stress shielding: Design versus materials versus interface. Clin. Orthop. Relat. Res. 274, 202–212. https://doi.org/10.1097/00003086-199201000-00020

Sutton, M., Wolters, W., Peters, W., Ranson, W., McNeill, S., 1983. Determination of displacements using an improved digital correlation method. Image Vis. Comput. 1, 133–139. https://doi.org/10.1016/0262-8856(83)90064-1

Sztefek, P., Vanleene, M., Olsson, R., Collinson, R., Pitsillides, A.A., Shefelbine, S., 2010. Using digital image correlation to determine bone surface strains during loading and after adaptation of the mouse tibia. J. Biomech. 43, 599–605. https://doi.org/10.1016/j.jbiomech.2009.10.042

Tayton, E., Evans, S., O'Doherty, D., 2010. Mapping the strain distribution on the proximal femur with titanium and flexible-stemmed implants using digital image correlation. J. Bone Jt. Surg. - Ser. B 92, 1176–1181. https://doi.org/10.1302/0301-620X.92B8.23553

Tonelli, L., Fortunato, A., Ceschini, L., 2020. CoCr alloy processed by Selective Laser Melting (SLM): effect of Laser Energy Density on microstructure, surface morphology,

and hardness. J. Manuf. Process. 52, 106–119. https://doi.org/10.1016/j.jmapro.2020.01.052

Van Bael, S., Chai, Y.C., Truscello, S., Moesen, M., Kerckhofs, G., Van Oosterwyck, H., Kruth, J.P., Schrooten, J., 2012. The effect of pore geometry on the in vitro biological behavior of human periosteum-derived cells seeded on selective laser-melted Ti6Al4V bone scaffolds. Acta Biomater. 8, 2824–2834. https://doi.org/10.1016/j.actbio.2012.04.001

Wang, D., Yang, Y., Liu, R., Xiao, D., Sun, J., 2013. Study on the designing rules and processability of porous structure based on selective laser melting (SLM). J. Mater. Process. Technol. 213, 1734–1742. https://doi.org/10.1016/j.jmatprotec.2013.05.001

Wolff, J., 1893. Das Gesetz der Transformation der Knochen. Dtsch. Medizinische Wochenschrift 19, 1222–1224. https://doi.org/10.1055/s-0028-1144106

Xin, X.Z., Xiang, N., Chen, J., Wei, B., 2012. In vitro biocompatibility of Co-Cr alloy fabricated by selective laser melting or traditional casting techniques. Mater. Lett. 88, 101–103. https://doi.org/10.1016/j.matlet.2012.08.032

Yan, C., Hao, L., Hussein, A., Young, P., 2015. Ti-6Al-4V triply periodic minimal surface structures for bone implants fabricated via selective laser melting. J. Mech. Behav. Biomed. Mater. 51, 61–73. https://doi.org/10.1016/j.jmbbm.2015.06.024

Zhang, D., Arola, D.D., 2004. Applications of digital image correlation to biological tissues. J. Biomed. Opt. 9, 691. https://doi.org/10.1117/1.1753270

Zhang, S., Wei, Q., Cheng, L., Li, S., Shi, Y., 2014. Effects of scan line spacing on pore characteristics and mechanical properties of porous Ti6Al4V implants fabricated by selective laser melting. Mater. Des. 63, 185–193.